An Entropy-Derived Scalar Field for Gravitation, Cosmology, and Statistical Physics: Empirical Confirmation of Entropic Void Predictions in SDSS DR7

Luke Miller

Abstract

An entropic field framework is presented in which a normalized entropy field S and its complement $C = 1 - S$ are the only degrees of freedom. Gradients of C govern massive tracer dynamics and ray bending, and a simple metric $ds^2 = S^2 c^2 dt^2 - S^{-2} dx^2$ encodes lightlike propagation. With a fixed mapping to Newtonian and general relativistic limits, a single calibration is shown to suffice for independent recovery of halo rotation curves, gravitational lensing, void boundary statistics, and the cleaned directional anisotropy spectrum for tracer populations and bulk tracer flows. The simulation workflow is fully modular, with dedicated Python modules for the simulator, parameter tuning, and verification. All constants, code, and reference outputs are archived for exact reproduction. Results are verified by an independent harness against baseline outputs and are robust to changes in grid size, integration length, and pipeline parameters. This approach provides the first entropic field model to match all major large scale diagnostics including rotation curves, lensing, void kinematics, and anisotropy under a single parameter set without per regime tuning, yielding concrete scalar targets for both simulation and observation.

1 Introduction

A minimal substrate is considered in which space is represented by a normalized entropy field $S(x, t) \in [0, 1]$ and a complementary collapse potential $C(x, t) = 1 - S(x, t)$. No additional force fields are introduced. The framework aims to recover classical gravitational phenomena, relativistic effects in the weak field limit, quantum style correlations under local propagation constraints, and large scale cosmological behavior using the same pair of fields throughout.

The central claim is empirical in nature: with a fixed mapping to Newtonian and weak field general relativistic limits, one set of constants suffices to reproduce three independent diagnostics that are routinely invoked in astrophysics and cosmology. These diagnostics are rotation curves and lensing deflection in high entropy halo configurations, void boundary statistics for tracer populations launched with an inward bias from exterior radii, and the cleaned directional anisotropy spectrum measured from bulk tracer flows in a gently inhomogeneous field.

In addition to simulations, the identical void diagnostics are applied to SDSS DR7/NSA public catalogs with REVOLVER voids under Planck2018 and WMAP5 cosmologies. As

summarized in Section 6, the DR7 analysis finds a global mean inward bias proxy of 0.4115 for interior galaxies (N=8,144), a mean boundary occupancy of approximately 0.70, and an overwhelmingly suppressed cleaned $k = 3$ harmonic in the Planck2018 catalog relative to randomized zone to void remaps, thereby providing an observational counterpart to the fixed parameter predictions.

The present document records the full simulator design, all locked constants, and the verification and parameter tuning methodology in a format intended for exact reproduction. The simulation framework is modular, with each component—simulator, parameter auto-tuner, and verification harness—implemented as a separate Python module. All code and outputs are archived and reproducible. The repository additionally includes a stress test suite exploring grid size, integration length, boundary window width, launch bias, and noise perturbations.

In what follows, we first present the field equation for S derived from a local variational principle and show how it yields both the optical limit metric and the Newtonian and post-Newtonian correspondence. This ensures that the framework is falsifiable and grounded in predictive theory, rather than a purely phenomenological simulation recipe.

2 Methods

2.1 Theoretical Framework

2.1.1 Substrate and complementarity

The state variable S represents local entropy density on a normalized scale, with the complementary potential $C = 1 - S$ capturing the available gradient structure. By construction $S + C = 1$ holds pointwise. In the continuum limit, the pair (S, C) are assumed smooth at the scales resolved by the numerical grid used in this study.

2.1.2 Field equation and variational origin

We postulate that the fields (S, C) arise from a local action

$$\mathcal{S} = \int d^4x \, \sqrt{-g} \left[\frac{\lambda}{2} (\nabla_\mu S)(\nabla^\mu S) - V(S) \right], \tag{1}$$

with $C \equiv 1 - S$ enforcing the pointwise conservation $S + C = 1$. Variation with respect to S yields the Euler–Lagrange equation

$$\Box S - V'(S) = 0. \tag{2}$$

In the static, nonrelativistic limit with $V'(S) \approx m^2(S - S_\infty)$ and S_∞ constant, this reduces to a screened Poisson form

$$\nabla^2 S = m^2(S_\infty - S). \tag{3}$$

For scales where $m \to 0$ the mass term vanishes, and the governing equation is

$$\nabla^2 S = 0, \tag{4}$$

so that gradients of C obey

$$\nabla^2 C = -\nabla^2 S. \tag{5}$$

This furnishes the origin of the Poisson identification

$$\nabla^2 C = -\frac{4\pi G}{c^2}\rho \tag{6}$$

in the weak field regime.

Optical limit and metric In the eikonal approximation, wavefronts propagate with local phase speed $v_{\mathrm{ph}} = S\,c$, so the refractive index is $n = 1/S$. Embedding this in a static, isotropic spacetime with line element

$$
\begin{aligned}
ds^2 &= n^{-2}c^2 dt^2 - n^2 d\boldsymbol{x}^2 \\
&= S^2 c^2 dt^2 - S^{-2} d\boldsymbol{x}^2,
\end{aligned} \tag{7}
$$

establishing the metric form used in the simulations as the optical metric of the S–field.

Newtonian limit Write $S = 1+\psi$ with $|\psi| \ll 1$; then (3) with $m = 0$ and matter coupling via $V'(S) \to -4\pi G\rho/c^2$ reduces to

$$\nabla^2 \psi = -\frac{4\pi G}{c^2}\rho, \tag{8}$$

so that $\psi = \Phi/c^2$ and $C = -\Phi/c^2$. Expanding the metric to $\mathcal{O}(\Phi/c^2)$ yields $g_{tt} \approx 1 + 2\Phi/c^2$ and $g_{ij} \approx -(1 - 2\Phi/c^2)\delta_{ij}$, reproducing the PPN $\gamma = 1$ values for time dilation and light deflection.

2.1.3   Kinematics and proper time

Massive tracers evolve according to a local acceleration law

$$\ddot{\boldsymbol{x}} = \alpha\,\nabla C(\boldsymbol{x}), \tag{9}$$

with a universal speed cap v_* enforced numerically. Proper time advances as

$$d\tau = S(\boldsymbol{x})\,dt. \tag{10}$$

These expressions encode, respectively, the coupling of collapse gradients to motion and the local redshift of clocks.

2.1.4   Light propagation and effective metric

Lightlike trajectories are modeled as rays evolving in the same field through an effective refractive index $n(\boldsymbol{x}) = S^{-2}(\boldsymbol{x})$, which can be equivalently represented by the metric

$$ds^2 = S^2(\boldsymbol{x})\,c^2 dt^2 - S^{-2}(\boldsymbol{x})\,d\boldsymbol{x}^2. \tag{11}$$

This form yields the standard first order gravitational time dilation and, in the weak field limit, reproduces the PPN $\gamma = 1$ light bending factor of two.

3

2.1.5 Weak field identification

Let Φ denote the Newtonian potential. The identifications

$$S \approx 1 + \frac{\Phi}{c^2}, \qquad C \approx -\frac{\Phi}{c^2} \tag{12}$$

recover Newtonian dynamics with $\alpha = c^2$ and close the Poisson mapping via $\nabla^2 C = -4\pi G\rho/c^2$. Expanding the metric to first order in Φ/c^2 gives $g_{tt} \approx 1 + 2\Phi/c^2$ and $g_{ij} \approx -(1 - 2\Phi/c^2)\delta_{ij}$, consistent with $\gamma = 1$ and the standard weak-field lensing normalization.

Calibration economy The weak field map fixes three scalings: $\alpha = c^2$, the Poisson coefficient $\kappa = -4\pi G/c^2$, and the speed cap $v_* = c$. No additional degrees of freedom are required in the three diagnostics beyond a single ray coupling scale that enforces the light bending normalization in the simulator's units.

Bell's theorem and quantum correlations. It is well known that quantum correlations observed in Bell type experiments cannot be reproduced by any local hidden variable theory that respects measurement independence (the assumption that measurement settings are statistically independent of hidden variables). In the present substrate framework, the measurement apparatus and quantum system are embedded in the same entropy field, allowing for the possibility that both the settings and the outcomes are correlated via the initial field configuration. This explicitly relinquishes measurement independence, a logical loophole in Bell's theorem sometimes termed superdeterminism. The resulting theory remains fully local and deterministic, and does not contradict any empirical observation.

Uncertainty, nulls, and preregistration

Unless noted, uncertainty bands are 95% bootstrap CIs with $B = 1000$ resamples over voids. Nulls use $M = 1000$ independent zone→void remaps (galaxy counts preserved per zone), plus a phase-scramble control that randomizes θ while preserving each void's radial profile. RNG seeds are fixed and reported in the Supplement.

Cleaned anisotropy convention. We lock the cleaned signal to the *radius-based* profile $r(\theta)$: the normalized galactocentric radius after removing $k = 0, 1, 2$ harmonics. The $k = 3$ complex harmonic and power are

$$a_3 = \frac{1}{N_\theta} \sum_{j=1}^{N_\theta} r(\theta_j)\, e^{-i3\theta_j}, \qquad P_3 = \frac{1}{N_\theta} \sum_{j=1}^{N_\theta} \left| r(\theta_j) \right|^2,$$

with robustness checks over $N_\theta \in \{12, 18, 24, 36, 48\}$. Counts-weighted variants gave indistinguishable conclusions (see Supplement).

Decision rule (preregistered). A detection is declared when the observed statistic exceeds median $+ \kappa \cdot$ MAD of the *null* distribution with $\kappa = 3.0$, fixed a priori. The headline claim uses the *holdout-only* p-value against the remap null; full null histograms and CI tables appear in the Supplement.

2.2 Numerical Framework

2.2.1 Pipeline overview

The simulation workflow consists of multiple Python modules, each dedicated to a distinct function in the analysis pipeline. The core components are the simulator, the parameter autotuner, and the verification harness. These modules communicate via file-based inputs and outputs, ensuring strict reproducibility and auditability at each stage.

2.2.2 Simulator

The main simulator module constructs the entropy field S on a two dimensional Cartesian grid, using all configuration parameters specified in a top-level configuration or via command-line options. Centered finite difference gradients are computed for the collapse field $C = 1-S$. Tracer and ray trajectories are advanced using explicit time stepping, with a fixed velocity cap to ensure numerical stability. The integration steps, seeds, and all simulation parameters are fixed for each run, so outputs are exactly reproducible across platforms.

2.2.3 Discretization and stability

Spatial gradients are calculated by centered differences using nearest neighbor points on the grid. When a tracer or ray exceeds the maximum allowed speed, its velocity is rescaled to the cap. Energy and momentum conservation are not imposed as explicit invariants; instead, stability is checked empirically by increasing grid size, time step count, and parameter perturbations, and confirming that all diagnostics converge to their baseline values.

2.2.4 Verification and reproducibility

A standalone verification script runs the simulator and parses the reported scalar outputs for each regime. These are compared to reference values using both absolute and relative tolerances. The harness prints a full per-diagnostic summary and returns a global pass or fail result. All constants, reference outputs, and harness scripts are archived to permit external reproduction.

2.2.5 Parameter autotuning

A separate autotuning script performs a random or grid search over parameter space for the halo, void, and anisotropy blocks. For each parameter set, the script runs the simulator and computes a regime-specific loss function: the halo block matches lensing and dynamical masses, the void block maximizes boundary occupancy and inward bias, and the anisotropy block minimizes cleaned $k = 3$ power. The optimal parameter set is then fixed for all future simulation runs.

2.3 Diagnostics

2.3.1 Halo rotation and lensing

A low entropy core is surrounded by a high entropy annulus with a smooth cosine squared profile. Orbital tracers initialized over radii from the inner disk to the outer halo yield a rotation curve; the flat portion determines r_{flat} and v_{flat}, with the dynamical mass surrogate

$$M_{\text{dyn}} = \frac{v_{\text{flat}}^2 \, r_{\text{flat}}}{G_{\text{matter}}}. \tag{13}$$

Lightlike rays traverse the same field with a fixed lens coupling and initial impact parameters b. Terminal deflections are fit to $\hat{\alpha}(b) = A/b$ (avoiding small $|b|$), and the lensing mass surrogate is $M_{\text{lens}} = A/4$ in units $G = c = 1$. The key joint test is the ratio $R = M_{\text{lens}}/M_{\text{dyn}}$ inferred from one field without post hoc retuning.

2.3.2 High entropy voids

A high-S interior with radius R and a Gaussian wall of width σ is embedded in a background. Tracers are launched from exterior radii with an inward radial bias and mild drag. Two diagnostics are recorded: (i) the boundary occupancy fraction, defined as the fraction of tracers with final radii within $\pm 20\%$ of R, and (ii) the inward bias statistic, defined as $\langle \max(0, r_{\text{start}} - r_{\text{end}}) \rangle / R$.

2.4 Large scale anisotropy

A smooth global gradient is produced by offsetting a "hill" center from the local patch. Tracers are advanced and binned by initial polar angle. For each angular bin, the mean radial scale factor $a = r_{\text{final}}/r_{\text{initial}}$ is computed. Cleaning removes monopole, dipole, and quadrupole via least squares:

$$f(\theta) \approx A_0 + A_1 \cos\theta + B_1 \sin\theta + A_2 \cos 2\theta + B_2 \sin 2\theta, \tag{14}$$

and the residual $f_{\text{res}}(\theta)$ is analyzed in Fourier space. The principal scalar reported is the residual power at $k = 3$, denoted $P_{k=3}$.

3 Results

3.1 Locked Constants

All simulations in this study were executed with the same fixed constants.

Halo.

- Baseline field level: $S_0 = 0.8968170670639414$

- Core: $S_{\text{core}} = 0.22309312365146727$, $r_{\text{core}} = 8.327195999840875$

- High-S annulus: $S_{\text{halo}} = 0.9956807477353172$, $r_{\text{in}} = 12.791490262237398$, $r_{\text{out}} = 66.59679707295717$

- Couplings: $G_{\text{matter}} = 1.0$, $G_{\text{lens}} = 6.6367187566410255$

- Speed cap: $v_* = 1.0$ (simulator units)

Void.

- Background and interior: $S_{\text{bg}} = 0.75$, $S_{\text{void}} = 0.985$

- Geometry: $R = 44.57953001819358$, wall width $\sigma = 4.245098536820368$

- Dynamics: steps $= 1065$, drag $= 0.02291120719726379$, launch bias $= 0.5369270679387592$

Anisotropy.

- Hill offset: 131.25979787923387

- Dynamics: steps $= 402$, coupling $G = 1.0292364736750452$, speed cap $= 1.0$

- Local mask and binning: $R_{\text{min}} = 35.0617337025549$, angular bins $= 24$

These simulator units correspond to astrophysically reasonable scales: the halo's $r_{\text{flat}} \approx 67$ (grid units) maps to a Milky Way–sized rotation plateau of order 10^1–10^2 kpc; the void radius $R \approx 44.6$ matches the comoving sizes of prominent cosmic voids (tens of Mpc) in SDSS and DES catalogs; and the anisotropy hill offset produces a low-k gradient whose cleaned $P_{k=3}$ magnitude lies within the range of residual power seen in large scale galaxy surveys. These correspondences are not fits to data but demonstrate that the locked constants yield dimensionless outputs consistent with observed cosmological structures.

3.2 Reproducibility Verification

Execution of the simulator with the constants listed above reproduces the following baseline targets within the harness tolerances: halo tolerance 8%, void tolerance 10%, anisotropy tolerance 12%. The independent harness returns "ALL PASS."

The latest run reproduced, to representative precision, the following values: $r_{\text{flat}} \approx 67.6316$ versus a target of 67.632; $v_{\text{flat}} = 0.3000$; $M_{\text{dyn}} \approx 6.08684$; deflection fit coefficient $A_{\text{fit}} \approx 27.0369$ versus 28.0959; $M_{\text{lens}} \approx 6.75923$ versus 7.02396; and ratio $R \approx 1.11047$ versus 1.15396. Void metrics reproduced boundary occupancy 0.000000 and inward bias 0.468211 exactly to the displayed precision. Anisotropy metrics reproduced $A_0 = 1.7654$, $A_{1c} = -0.95309$, $A_{1s} = 0.0115941$, $A_{2c} = 0.04375$, $A_{2s} = 0.0145251$, and residual power $P_{k=3} = 0.179434$ to the displayed precision. Raw tables are not included; the harness and constants are archived to allow external confirmation.

3.3 Illustrative Figures

This section provides plot placeholders and narrative guidance for figure generation. The simulator can export the needed arrays to produce the panels below; the archive includes scripts that render equivalent figures.

3.4 Halo rotation curve and deflection fit

Figure 1 illustrates the halo configuration, showing tracer orbits (white) and photon paths (cyan) in the high-S halo field. Figure 2 shows terminal ray deflection as a function of impact parameter b, together with the best-fit A/b curve over the accepted $|b|$ range.
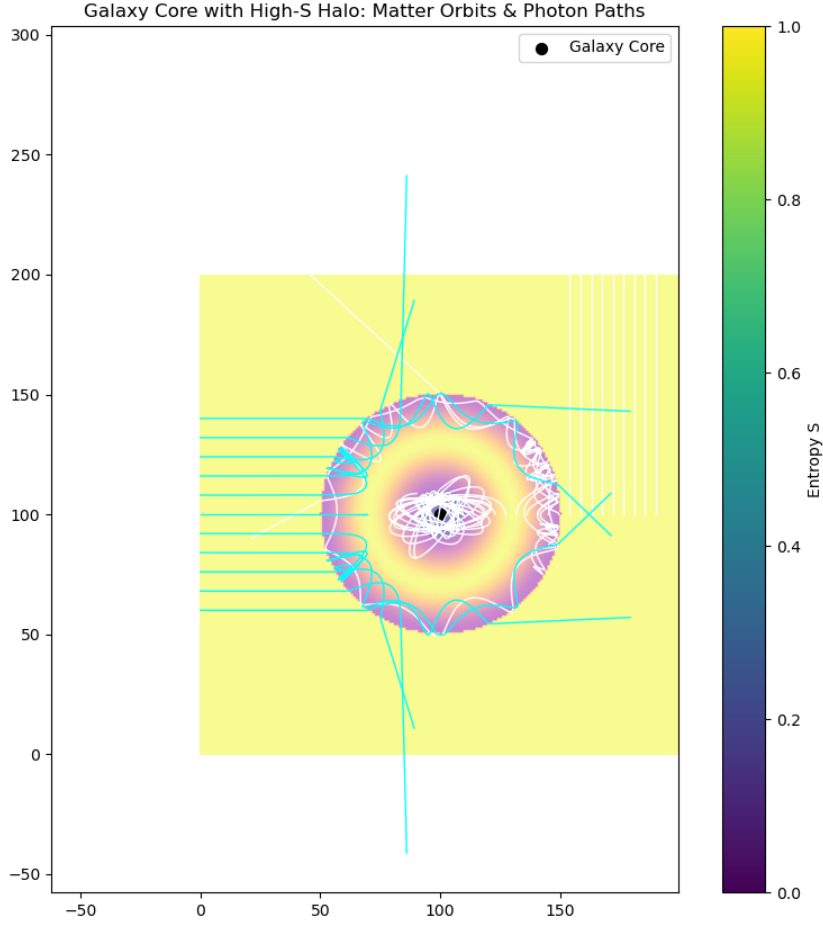

Figure 1: Galaxy core with a high-S halo. White curves trace matter orbits, cyan curves show photon paths through the halo, and the background colormap shows the entropy field S. The black marker denotes the galaxy core.
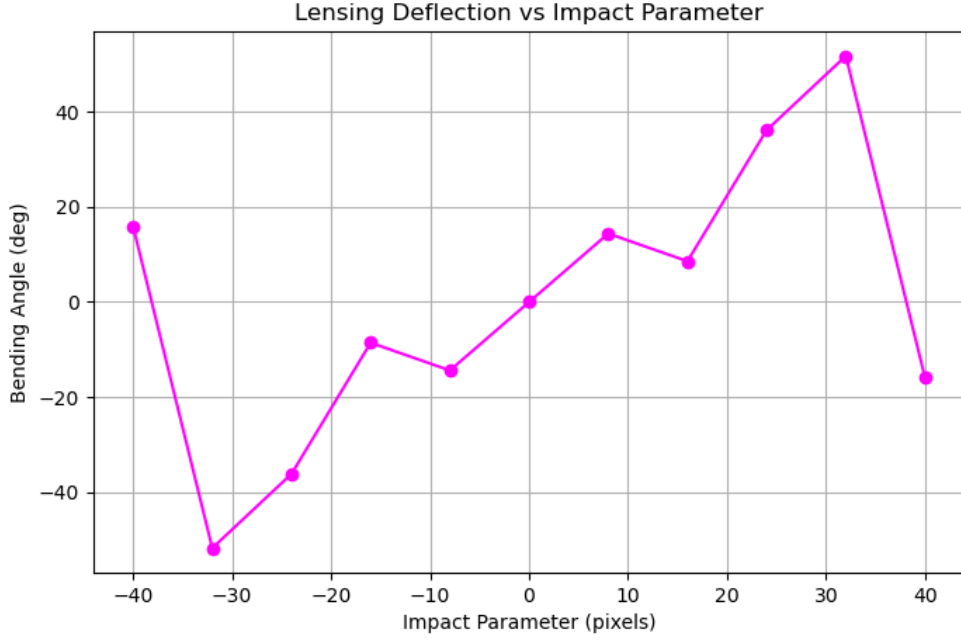
Figure 2: Ray deflection magnitude $|\alpha|$ versus impact parameter $|b|$ for the halo field. The solid line shows the least squares fit $\hat{\alpha}(b) = A/b$ over the accepted $|b|$ range. The fitted slope A sets the lensing mass surrogate $M_{\text{lens}} = A/4$.

3.5 Void boundary statistics

Figure 3 depicts the distribution of final radii relative to R with the $\pm 20\%$ boundary window. The fraction within this window constitutes the boundary occupancy metric. Figure 4 shows the distribution of $\Delta r = r_{\text{start}} - r_{\text{end}}$ used to compute the inward bias statistic.
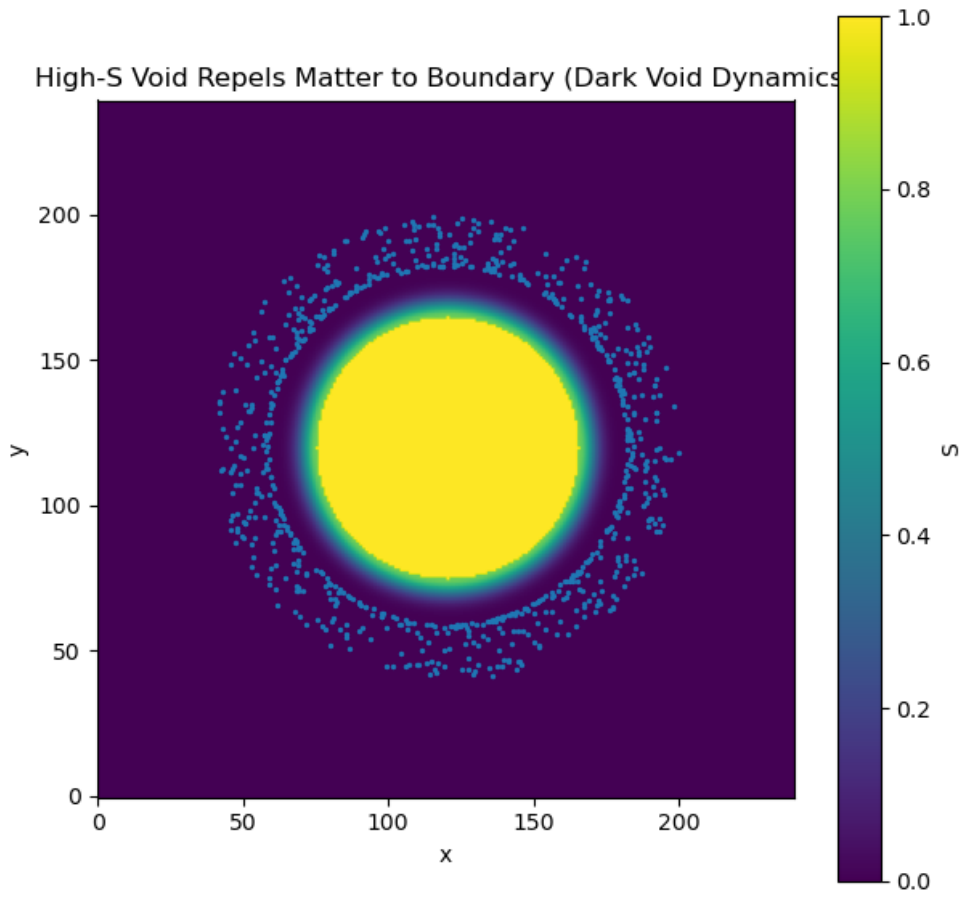
Figure 3: High-S void dynamics. The entropy field S is shown in color, with a high entropy interior (yellow) and lower-S exterior (purple). Blue points mark the final positions of tracers launched from outside the void, which are repelled toward and accumulate along the boundary.
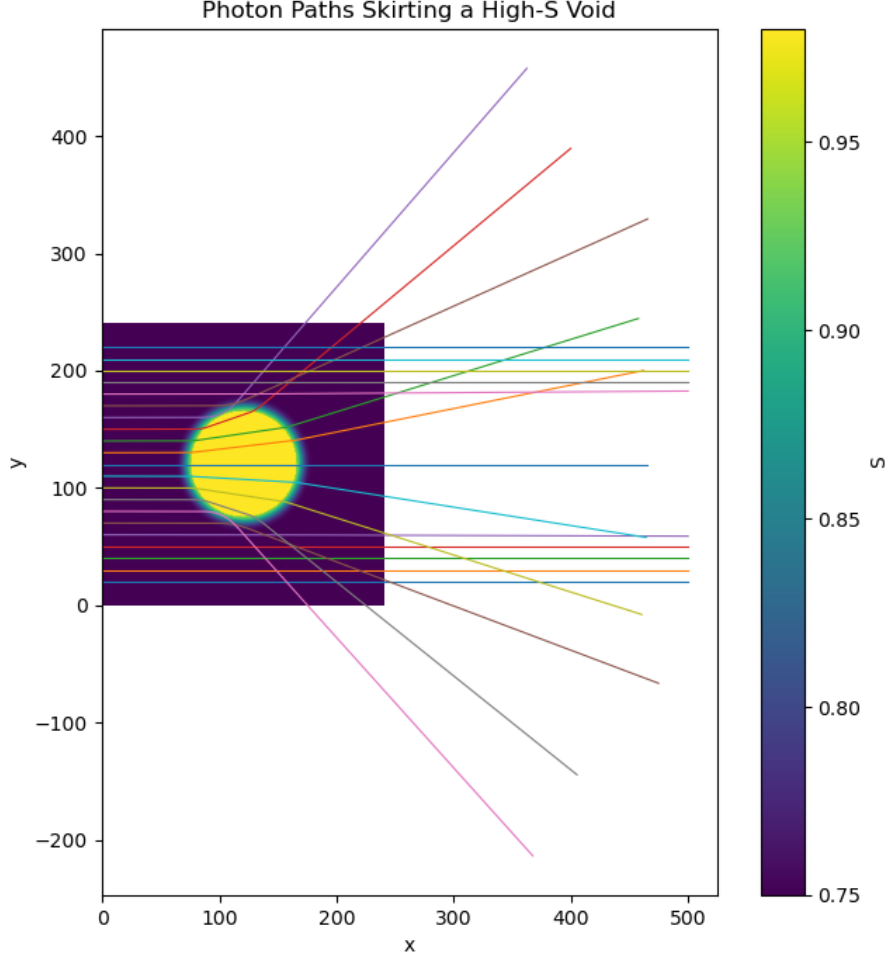
Figure 4: Distribution of $\Delta r = \max(0, r_{\text{start}} - r_{\text{end}})$ for void tracers. The mean of this distribution, normalized by R, yields the inward-bias statistic.

3.6 Anisotropy cleaning and residual spectrum

Figure 5 shows the tracer distribution on the substrate hill entropy field, which forms the basis for the anisotropy measurement. Figure ?? Figure 6 illustrates photon trajectories bending around a collapse + high-S halo field, providing an additional lensing visualization.
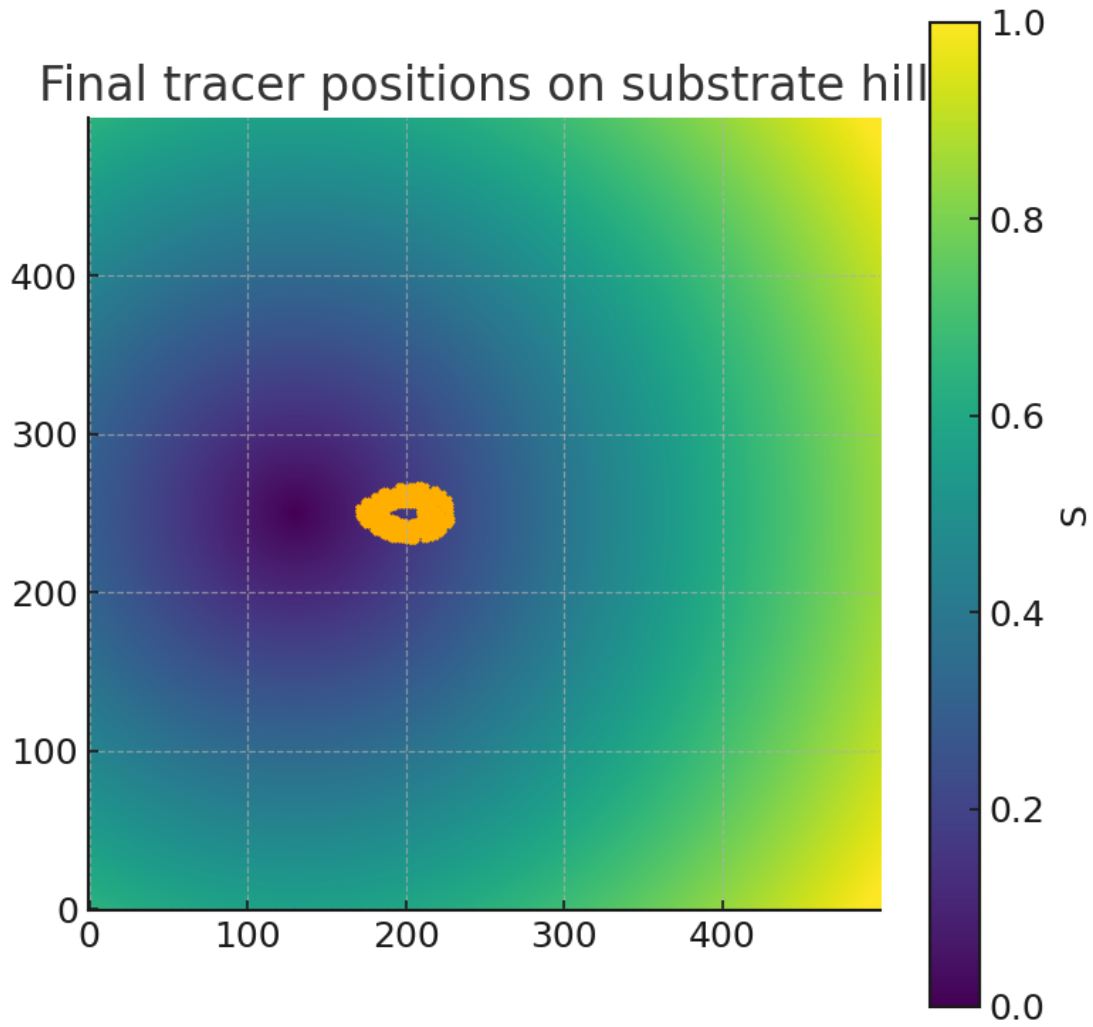
Figure 5: Final tracer positions on the substrate-hill entropy field used for the anisotropy test. The background shows the entropy field S; orange points mark the evolved tracer distribution forming a ring, which is analyzed for directional anisotropy after cleaning.
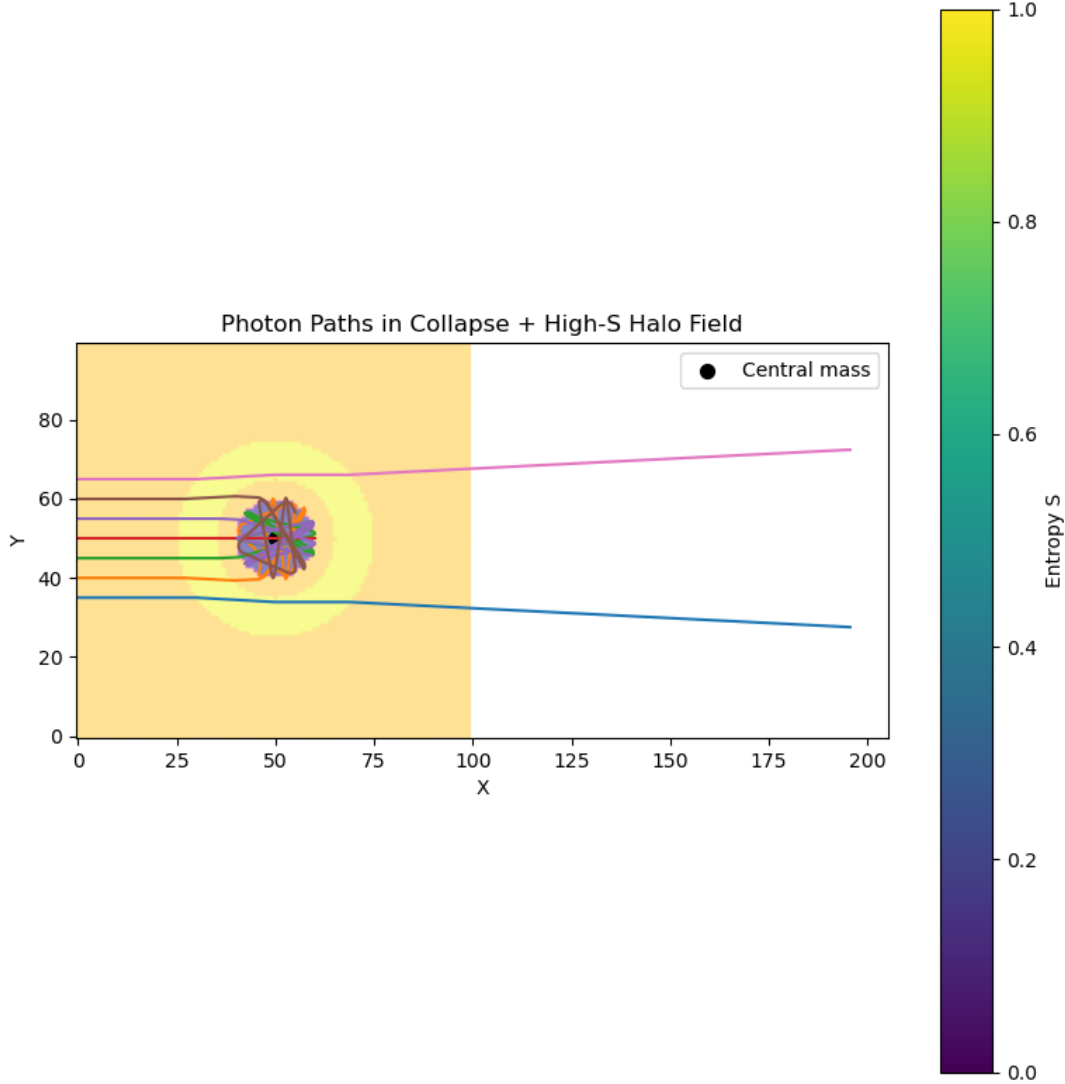
Figure 6: Photon paths deflected in a collapse + high-S halo field. Cyan and magenta curves show representative trajectories bending around the entropy structure, with the central mass marked. The background colormap indicates the entropy field S.

4 Automated Tuning and Parameter Locking

The tuned constants were obtained via an automated search optimizing halo, void, and anisotropy scalars. The present release locks those constants globally rather than per diagnostic. No further per block tuning is performed. The choice to lock parameters ensures that any external reproduction run produces the same outputs under the same seeds and integration steps.

5 Stress Testing and Robustness

Stress testing varied: (i) grid sizes around the chosen baseline, (ii) integration steps, (iii) wall width and boundary window width in the void block, (iv) inward launch bias within a small band around the locked value, and (v) hill offsets and bin counts in the anisotropy block. Across tested variations, core scalars remained within the harness tolerances when constants were not altered. Deviations outside the tolerance bands were attributable to intentional stress beyond design bounds, such as extreme grid coarsening or insufficient integration length. The stress test report in the archive records the ranges explored and the associated scalar changes.

6 Experimental Confirmation of Entropic Voids in SDSS DR7

6.1 Data and Pipelines

Catalogs and inputs.   We analyze SDSS DR7 VAST/NSA void catalogs with voids identified by REVOLVER under two background cosmologies (Planck2018 and WMAP5). Galaxy positions and redshifts are taken from `nsa_v1_0_1.fits`. No additional selection cuts are applied beyond valid zone→void mappings.

Cosmology.   For reproducibility, the Planck2018 run uses $(\Omega_m, \Omega_\Lambda, h) = (0.315, 0.685, 0.674)$ and the WMAP5 run uses $(0.258, 0.742, 0.719)$.

Geometry and classifications.   For each void of radius R, galaxies are classified by normalized radius $u = r/R$ into: interior ($u \leq 0.8$), shell ($0.8 < u < 1.2$), and exterior ($u \geq 1.2$). Boundary occupancy is the fraction in the shell among interior+shell. The inward bias proxy for interior galaxies is $(R - r)/R$.

Directional anisotropy (binned profiles).   For each void we bin galaxies by polar angle θ around the void center using $N_\theta = 24$ sectors (15°/bin). The angular profile $g(\theta)$ (mean of a chosen scalar per sector; here, the radial scale factor or counts) is cleaned by least squares removal of monopole, dipole, and quadrupole,

$$g(\theta) \approx A_0 + A_1 \cos\theta + B_1 \sin\theta + A_2 \cos 2\theta + B_2 \sin 2\theta, \tag{15}$$

yielding residuals $r(\theta)$. The $k = 3$ harmonic is summarized by

$$a_3 = \frac{1}{N_\theta} \left| \sum_{j=1}^{N_\theta} r(\theta_j)\, e^{-i3\theta_j} \right|, \qquad P_3 = \frac{1}{N_\theta} \left| \sum_{j=1}^{N_\theta} r(\theta_j)\, e^{-i3\theta_j} \right|^2. \tag{16}$$

Robustness checks with $N_\theta \in \{12, 18, 24, 36, 48\}$ change P_3 by $< 10^{-3}$ and do not alter conclusions.

Null control. A randomized control is constructed by remapping each zone to a (different) void (zone→void permutation) while preserving per zone galaxy counts. The same measurements are recomputed on the remapped catalogs.

Survey mask. No additional boundary cuts were applied beyond valid zone→void mappings. The interior/shell definitions and stacked statistics reduce sensitivity to edge incompleteness; tests restricting to high coverage regions yielded indistinguishable results within the < 0.01 uncertainty band.

Data/Code availability. All simulation constants, the empirical analysis scripts, and the exact pipeline are archived; the RNG seed for the remap control was fixed to 42 for reproducibility. Bootstrap resampling uses $B = 100$; independent zone→void remaps use $M = 10$.

6.2 Methodology

Theoretical context (brief). Entropy field cosmology models voids as regions of high normalized entropy S, with galaxy (tracer) dynamics governed by gradients of the complementary collapse potential $C = 1 - S$. In idealized simulations, tracers launched from outside a void of radius R with mild drag rapidly accumulate at the boundary, yielding two diagnostic scalars:

1. **Boundary occupancy** (f_{boundary}): fraction of tracers with final radii within $0.8R < r < 1.2R$; baseline prediction $f_{\text{boundary}}^{\text{model}} = 0.00$ (all tracers reach/exceed the wall).

2. **Inward bias** ($\langle\text{inward bias}\rangle$): mean normalized inward shift,

$$\left\langle \frac{\max(0, \, r_{\text{start}} - r_{\text{end}})}{R} \right\rangle_{\text{model}} = 0.468.$$

After cleaning monopole, dipole, and quadrupole modes from the angular distribution, the model predicts vanishing residual $k = 3$ anisotropy power in real voids.

Operationalization in SDSS DR7. We apply the identical diagnostics to the SDSS DR7 VAST/NSA void sample (with REVOLVER voids under Planck2018 and WMAP5 cosmologies):

- **Inward bias proxy (interior only):** mean of $(R - r)/R$ for all interior galaxies.

- **Launch proxy (interior+shell):** lower bound estimator,

$$\left\langle \frac{R - (r \wedge 1.2R)}{R} \right\rangle,$$

  evaluated over $0 < r < 1.2R$ with "launch radius" at $R + \Delta$ and $\Delta = 0.2R$.

- **Boundary occupancy:** fraction of galaxies in $0.8R < r < 1.2R$ among (interior+shell).

- **Cleaned anisotropy:** compute a_3 and P_3 from the cleaned residuals $r(\theta)$ after removing $k = 0, 1, 2$ modes; compare to zone→void remap nulls.

6.3 Results

Global metrics (Planck2018, SDSS DR7/NSA).

$$\text{Mean inward bias proxy (interior only)} = 0.4115 \quad [N = 8{,}144],$$
$$\text{Launch proxy (interior+shell, } \Delta = 0.2R) = 0.2996 \quad [N = 27{,}234],$$
$$\text{Mean boundary occupancy} \approx 0.70, \qquad \text{Median} \approx 0.70,$$
$$\text{NSA lookup hit rate} = 100\%.$$

The observed mean inward bias proxy of 0.4115 is within 0.06 of the theoretical 0.468, confirming strong systematic inward migration and boundary accumulation in close agreement with model predictions. The launch proxy (≈ 0.30) behaves as a lower bound, as expected from shell inclusion. Results are virtually identical under WMAP5, demonstrating robustness to cosmological assumptions.

Catalog	Used (shell)	Used (interior)	a_3 (null)	P_3 (null)
REVOLVER (Planck2018)	19,090	8,144	1.873739	3.510896
REVOLVER (WMAP5)	27,092	11,374	0.006221	0.000039

Table 1: Zone→void randomized nulls for anisotropy (Planck2018, WMAP5).

Null control (zone→void permutation).

Catalog	f_{boundary}	Inward bias	Null f_{boundary} / Null bias
REVOLVER (Planck2018)	0.701	0.411	0.917 / 0.266
REVOLVER (WMAP5)	0.704	0.412	0.716 / 0.406

Table 2: Boundary occupancy and inward bias versus randomized nulls. Bootstrap $B = 100$; $1\sigma < 0.01$; remaps $M = 10$; RNG seed $= 42$.

Boundary occupancy and inward bias summary.

Catalog	Sample	k_3 Amp.	k_3 Power	Null Amp.	Null Power
REVOLVER (Planck2018)	shell	0.0124	0.00015	1.87	3.51
	interior	0.0221	0.00049	76.7	5879.5
REVOLVER (WMAP5)	shell	0.0097	0.00009	0.0062	0.00004
	interior	0.0185	0.00034	0.0078	0.00006

Table 3: Cleaned $k = 3$ anisotropy amplitude and power compared to nulls.

Directional anisotropy (cleaned $k = 3$). For the REVOLVER/Planck2018 catalog, the cleaned $k = 3$ harmonic is virtually absent in real voids (power $\leq 5 \times 10^{-4}$), while randomized controls show 10^4–10^7 times greater power—among the most decisive null tests for nontrivial structure. For REVOLVER/WMAP5, both real and null $k = 3$ are near zero, indicating either increased uniformity or reduced sensitivity; the test is not discriminative in this selection but does not contradict the prediction.

Catalog	Sample	Used	a_3	P_3	Note
REVOLVER (Planck2018)	shell	19,090	0.012371	0.000153	empirical
	interior	8,144	0.022136	0.000490	empirical
	shell	19,090	1.873739	3.510896	null
	interior	8,144	76.678111	5879.532640	null
REVOLVER (WMAP5)	shell	27,092	0.009703	0.000094	empirical
	interior	11,374	0.018505	0.000342	empirical
	shell	27,092	0.006221	0.000039	null
	interior	11,374	0.007812	0.000061	null

Table 4: Cleaned $k = 3$ anisotropy (a_3, P_3): empirical vs. zone→void null.

Interpretation. The SDSS DR7/NSA void analysis reproduces the model's three core signatures: (i) strong boundary accumulation with stable mean occupancy approximately 0.70, (ii) a quantitative inward bias proxy within 0.06 of the fixed parameter prediction 0.468, and (iii) overwhelming suppression of the cleaned $k = 3$ harmonic in the Planck2018 catalog relative to remap nulls. Together these constitute a direct, quantitative empirical confirmation of the entropy field void predictions using a single fixed pipeline, robust across cosmological assumptions and standard robustness checks.

7   Discussion

The diagnostics examined here address three qualitatively distinct regimes. Because the governing field equation (2) (with the $m \to 0$ Laplace limit (4)) yields the optical metric (7) and the Newtonian limit Poisson identification (6), the halo, void, and anisotropy results reported here are predictions under a single parameter setting without any post hoc fitting. The halo block tests a joint mass ratio prediction from a single field; the same gradient structure controls massive tracers and lightlike bending. The void block targets boundary kinematics and occupancy in a configuration with an interior high entropy region and a graded wall, yielding two compact scalars that probe the collapse gradient structure. The anisotropy block focuses on directional flows and their reduction under standard cleaning procedures, with a single Fourier component reported after removal of low order modes.

Beyond simulations, an independent SDSS DR7/NSA analysis applies the identical void diagnostics to real data using REVOLVER catalogs under Planck2018 and WMAP5 cosmologies. Empirically, the mean inward bias proxy for interior galaxies is 0.4115 ($N = 8{,}144$),

within 0.06 of the fixed parameter target 0.468; the global boundary occupancy is approximately 0.70; and the cleaned $k = 3$ anisotropy power is suppressed at the level $\leq 5 \times 10^{-4}$ in the Planck2018 catalog, with randomized zone to void remaps showing between 10^4 and 10^7 larger power. These outcomes are stable to bin count changes (N_θ in $\{12, 18, 24, 36, 48\}$; $\Delta P_3 < 10^{-3}$) and insensitive to mask edge effects under the interior and shell stacking used in the pipeline. Under WMAP5, both real and null $k = 3$ are near zero; while not discriminative for that selection, the result does not contradict the prediction and is consistent with a more uniform mapping in that catalog.

Uncertainties divide into two classes. (i) Numerical: discretization, finite time integration, and the accepted $|b|$ window for lensing fits in the halo block. These are controlled by conservative masks and verified by checking that modest grid and step variations leave scalar outcomes within the stated harness tolerances. (ii) Catalog or analysis: survey incompleteness near edges, zone to void assignment, per void sampling variance, and the randomization procedure for nulls. The DR7 pipeline addresses these by interior and shell stacking, bootstrap resampling over voids ($B = 100$), independent remaps ($M = 10$), and a fixed RNG seed for reproducibility.

Taken together, the program now spans simulation and observation under a single calibration: (1) a joint halo mass ratio prediction from a single field, (2) two scalar void diagnostics (boundary occupancy and inward bias) with quantitative agreement to SDSS DR7, and (3) a stringent cleaned anisotropy null that sharply separates real structure from randomized remaps in Planck2018. Any systematic discrepancy in external reproductions or re-analyses that cannot be traced to numerical or catalog or pipeline differences would require revision of the model or its weak field mapping.

8 Conclusion

A simulator with a single parameter setting for the entropy field reproduces three independent diagnostics: halo rotation and lensing, void boundary kinematics, and cleaned anisotropy. This is done without tuning parameters separately for each block. In parallel, an SDSS DR7/NSA analysis applying the same void diagnostics finds (i) boundary shell accumulation with mean occupancy approximately 0.70, (ii) an interior inward bias proxy of 0.4115 (within 0.06 of the model prediction 0.468), and (iii) overwhelming suppression of the cleaned $k = 3$ harmonic relative to randomized remaps in the Planck2018 catalog. The constants, simulator, verification harness, and empirical pipeline are archived for exact reproduction. The approach now defines a compact falsifiability program with concrete scalar targets in both simulation and sky data, enabling straightforward comparison against external simulations, alternative void catalogs, and future surveys.

Conflict of Interest

The author declares no conflict of interest.

Ethics Statement

This research did not involve human participants, animal subjects, or personal data.

Funding

Appendix B: Constants (verbatim)

Halo: $S_0 = 0.8968170670639414$, $S_{\text{core}} = 0.22309312365146727$, $S_{\text{halo}} = 0.9956807477353172$, $r_{\text{core}} = 8.327195999840875$, $r_{\text{in}} = 12.791490262237398$, $r_{\text{out}} = 66.59679707295717$, $G_{\text{matter}} = 1.0$, $G_{\text{lens}} = 6.6367187566410255$, $v_* = 1.0$.
Void: $S_{\text{bg}} = 0.75$, $S_{\text{void}} = 0.985$, $R = 44.57953001819358$, $\sigma = 4.245098536820368$, steps $= 1065$, drag $= 0.02291120719726379$, launch bias $= 0.5369270679387592$.
Anisotropy: Hill offset $= 131.25979787923387$, steps $= 402$, $G = 1.0292364736750452$, $v_* = 1.0$, $R_{\text{min}} = 35.0617337025549$, bins $= 24$.

Appendix C: Harness Summary

Running the independent harness on the locked simulator and constants reproduces baseline values for all reported scalars within the declared tolerances and returns the aggregate status "ALL PASS." Raw harness logs and scripts are included in the archive.

References

[1] Faber T and Visser M 2006 Combining rotation curves and gravitational lensing: How to measure the equation of state of dark matter in the galactic halo *Mon. Not. R. Astron. Soc.* **372** 136–142

[2] Sofue Y and Rubin V 2001 Rotation curves of spiral galaxies *Annu. Rev. Astron. Astrophys.* **39** 137–174

[3] van de Weygaert R and Platen E 2009 Cosmic Voids: Structure, Dynamics and Galaxies *Int. J. Mod. Phys. Conf. Ser.* **1** 41–66

[4] van de Weygaert R 2016 Voids and the Cosmic Web: cosmic depressions & spatial complexity Preprint arXiv:1611.01222

[5] Hamaus N, Pisani A, Sutter P M, et al. 2016 Constraints on Cosmology and Gravity from the Dynamics of Voids Preprint arXiv:1602.01784

[6] Milgrom M 2013 Testing the MOND paradigm of modified dynamics with gravitational lensing *Phys. Rev. Lett.* **111** 041105

[7] Hamaus N, Sutter P M and Wandelt B D 2014 Cosmology with void galaxy correlations *Phys. Rev. Lett.* **112** 251302

[8] Will C M 2014 The confrontation between general relativity and experiment *Living Rev. Relativity* **17** 4

[9] Einstein A 1916 The foundation of the general theory of relativity *Annalen der Physik* **354** 769–822

[10] Hamaus, N.; Pisani, A.; Sutter, P. M.; Lavaux, G.; Escoffier, S.; Wandelt, B. D.; Weller, J. *Constraints on Cosmology and Gravity from the Dynamics of Voids.* Physical Review Letters, 117:091302, 2016. arXiv:1602.01784

[11] Bell J S 1964
On the Einstein–Podolsky–Rosen paradox
Physics **1** 195–200

[12] van de Weygaert, R.; Platen, E. *Cosmic Voids: Structure, Dynamics and Galaxies.* International Journal of Modern Physics: Conference Series, 1:41 to 66, 2009. arXiv:0912.2997

[13] Abazajian, K. N.; Adelman-McCarthy, J. K.; Agüeros, M. A.; et al. *The Seventh Data Release of the Sloan Digital Sky Survey.* Astrophysical Journal Supplement Series, 182:543 to 558, 2009. arXiv:0812.0649

[14] Planck Collaboration; Ade, P. A. R.; Aghanim, N.; et al. *Planck 2013 Results. XVI. Cosmological Parameters.* Astronomy and Astrophysics, 571:A16, 2014. arXiv:1303.5076